Geomechanics and Engineering, *Vol. 20, No. 3 (2020) 175-189*
DOI: https://doi.org/10.12989/gae.2020.20.3.175

A set of failure variables for analyzing stability of slopes and tunnels

Jun-Mo Kim*[1,2], Sungho Lee[1], Jai-Yong Park[1], Jung-Hwi Kihm[3] and Sangho Park[4]

[1]*School of Earth and Environmental Sciences, Seoul National University, Seoul 08826, Republic of Korea*
[2]*GeoLab, Seoul 08787, Republic of Korea*
[3]*Department of Renewable Energy and Resources, Jungwon University, Goesan-Gun 28024, Republic of Korea*
[4]*School of Mechanical Engineering, Chungnam National University, Daejeon 34134, Republic of Korea*

(Received February 20, 2019, Revised November 3, 2019, Accepted November 4, 2019)

Abstract. A set of relatively simple five local shear and tension failure variables is presented and then implemented into a generalized poroelastic hydromechanical numerical model to analyze failure potential and stability of variably saturated geologic media. These five local shear and tension failure variables are formulated from geometrical relationships between the Mohr circle and the Mohr-Coulomb failure criterion superimposed with the tension cutoff, which approximate together the Mohr effective stress failure envelope. Finally, fully coupled groundwater flow and land deformation in two variably saturated geologic media, which are associated with a slope (Case 1) and a tunnel (Case 2), respectively, and their failure potential and stability are simulated using the resultant hydromechanical numerical model. The numerical simulation results of both cases show that shear and tension failure potential and stability of variably saturated geologic media can be analyzed numerically simply and efficiently and even better by using the five local shear and tension failure variables as a set than by using the conventional factors of safety against shear and tension failures only.

Keywords: variably saturated geologic media; slopes; tunnels; groundwater flow; land deformation; failure potential; stability; local shear and tension failure variables; poroelastic hydromechanical numerical analyses

1. Introduction

It has been realized that hydromechanical interaction between the groundwater flow field and the land (i.e., solid skeleton or geologic medium) deformation field plays important roles in controlling various geological, hydrogeological, and geomechanical processes (Neuzil 2003). Land deformation due to groundwater pumping, which acts as a hydraulic stress, is but one example. Another example is excessive pore water pressure generation due to physical loading, which acts as a mechanical stress. Since the pioneering work of Biot (1941), such hydromechanical phenomena have been better explained through poroelasticity theory or the poroelastic consolidation theory than by the conventional theory of solid skeleton deformation that is forced to be decoupled from groundwater flow. Poroelasticity theory has also been further developed for the entire saturated-unsaturated water flow regime by others (Verruijt 1969, Safai and Pinder 1979, Bear and Corapcioglu 1981a, Noorishad *et al*. 1982, Kim 1996, Kim and Parizek 1997, Kim *et al*. 1997, Kim and Parizek 1999a, 1999b, Kim 2000, 2003, 2004, 2005, Kim and Parizek 2005) using the modified effective stress concept (Terzaghi 1925, Biot 1941, Bishop and Blight 1963, Nur and Byerlee 1971, Carroll 1979, Thompson and Willis 1991, Cheng 1997, Kim 2004).

On the basis of Biot's poroelastic consolidation theory, a variety of poroelastic numerical simulations have been performed to evaluate groundwater flow and land deformation in geologic media, which are either fully or partially saturated with water, due to various causes such as groundwater pumping (Safai and Pinder 1979, Lewis *et al*. 1991, Yeh *et al*. 1996, Kim and Parizek 1997, Kim and Parizek 1999a, 1999b, Kim 2005, Kim and Parizek 2005), surface loading (Sandhu and Wilson 1969, Christian *et al*. 1972, Ghaboussi and Wilson 1973, Cui *et al*. 1996, Kim 2000), subsurface coal mining (Girrens *et al*. 1981, Bai and Elsworth 1991, Ouyang and Elsworth 1993, Bai and Elsworth 1994, Kim *et al*. 1997), and others. However, such poroelastic numerical simulations do not consider failure potential and stability of geologic media. Failure potential and stability analyses may not be particularly significant in the above-mentioned poroelastic numerical simulations but can be essentially critical in poroelastic numerical simulations of geologic media associated with slopes and tunnels.

The Mohr-Coulomb failure criterion (Coulomb 1776, Mohr 1900) has still so far become the most practical and popular means for analyzing failure potential and stability of geologic media associated with various engineering works such as slopes (e.g., Tu *et al*. 2016, Kim and Jeong 2017, Tran *et al*. 2019), tunnels (e.g., Khezri *et al*. 2016, Zheng *et al*. 2017, Yu 2018), foundations (e.g., Ardeshiri-Lajimi *et al*. 2016, Lee *et al*. 2016, Ukritchon *et al*. 2016), and embankments (e.g., Wang *et al*. 2016, Zhang *et al*. 2017, Balaban and Onur 2018). Owing to its historical development and simplicity, most of these conventional stability analyses used to calculate the factor of safety against shear failure, which is expressed in terms of the

*Corresponding author, Ph.D.
E-mail: junmokim@snu.ac.kr

ISSN: 2005-307X (Print), 2092-6219 (Online)

cohesion and the angle of internal friction. However, the Mohr-Coulomb failure criterion has been mainly focused on the shear failure only. As a result, the related application studies such as the limit equilibrium methods for slope stability analysis (Das 1994, Huang 2014) and the principal and shear stress methods for tunnel stability analysis (Jaeger and Cook 1979, Goodman 1989) have analyzed stability of geologic media in terms of the shear strength or the factor of safety against shear failure only. In contrast to the shear strength and the shear failure, the tensile strength and the tension failure have not been properly considered in such conventional stability analyses because appropriate tension failure variables (parameters) have not yet been presented. In addition, using the factor of safety against shear failure alone as in the conventional stability analyses, it is practically impossible to determine which one between the shear and tension failures actually takes place or not at a given location within geologic media, and thus one cannot evaluate rigorously failure potential and stability of geologic media under various stress field conditions. For instance, if the minimum principal effective stress is smaller than the tensile strength at a location, the tension failure occurs there instead of the shear failure even though the factor of safety against shear failure is smaller than unity. It strongly suggests that the tensile strength should also be considered as well as the shear strength in evaluating failure potential and stability of geologic media even in cases of high deviatoric or shear stress conditions. Thus, a set of new local shear and tension failure variables that can consider both shear and tensile strengths is essentially necessary for better illustration and more rigorous analyses of failure potential and stability of geologic media associated with slopes and tunnels.

In the limit equilibrium methods for slope stability analysis (Das 1994, Huang 2014), several circular surfaces are drawn arbitrarily first within a slope. The shear stress on each surface is then calculated using the moment or force balance and compared with the shear strength assigned. Finally, a surface that has the minimum value of the global factor of safety, which is defined as the ratio of the shear strength to the shear stress on it, is chosen as a potential shear failure surface through a trial and error procedure. However, the limit equilibrium methods assume the shape and location of the potential failure surface rather than determining them by analysis. As a result, one can produce inconsistent estimations for the shape and location of the potential failure surface and consequently the value of the global factor of safety with another's results depending on particular limit equilibrium methods they adopt. In addition, the limit equilibrium methods assume the uniform localization of shear stresses along the potential failure surface, but the shear stresses are not actually uniformly mobilized on its whole length. On the other hand, in the principal and shear stress methods for tunnel stability analysis (Jaeger and Cook 1979, Goodman 1989), spatial distribution of the principal or shear stress around a tunnel is determined first from field measurement or numerical simulation. It is then compared with the shear strength assigned. Finally, a region where the deviatoric or shear stress exceeds the shear strength or a specific value is chosen as an unstable zone. However, the principal and shear stress methods cannot delineate the potential shear failure zone since it does not always coincide spatially with such a high deviatoric or shear stress region (i.e., unstable zone) as mentioned in the preceding paragraph. Thus, a set of new local shear and tension failure variables that can consider both shear and tensile strengths is highly desirable for more realistic determination of the shape and location of a potential failure surface or zone under a stress field condition in geologic media associated with slopes and tunnels. In that case, the potential shear failure surface or zone, which is determined by using such a set of new local shear and tension failure variables, may have mostly a noncircular (curved) or irregular shape, which is more realistic, rather than a circular or regular shape, which is too ideal.

The first objective of this study is to present a set of relatively simple local shear and tension failure variables and to implement it into a generalized poroelastic hydromechanical numerical model, which can also handle both unsaturated water flow and rainfall-infiltration-seepage processes. The second objective of this study is to simulate fully coupled groundwater flow and land deformation in variably saturated geologic media associated with a slope (Case 1) and a tunnel (Case 2) and to analyze their failure potential and stability using the resultant hydromechanical numerical model. From a practical point of view, a quantitative understanding of fully coupled groundwater flow and land deformation and a simultaneous evaluation of both shear and tension failure potential may provide improved guidelines for controlling groundwater flow in deforming variably saturated geologic media associated with slopes and tunnels to maintain or increase the stability of such engineering works within the geologic media.

2. Local shear and tension failure variables

Considering the pore fluid (i.e., water and air) pressure via the above-mentioned modified effective stress concept, a saturated-unsaturated soil or rock (i.e., geologic medium or solid skeleton) fails under a specific combination of the maximum and minimum principal (deformation-producing) effective stresses σ'_1 and σ'_3 (for convenience, positive for compression and thus $\sigma'_1 \geq \sigma'_3$) (Coulomb 1776, Mohr 1900). This means that the failure does not occur under either maximum effective normal stress or maximum shear stress alone acting on a surface, but it takes place under a critical combination of the effective normal stress σ' (positive for compression) and the shear stress τ on the surface. Thus, the functional relationship between the effective normal stress and the shear stress on a failure surface can be expressed as follows (Jaeger and Cook 1979, Das 1994):

$$|\tau| = \tau_s = f(\sigma') \tag{1}$$

where the sign of the shear stress only affects the direction of sliding, and hence only the magnitude of the shear stress is in question (i.e., $|\tau| = \tau_s$), and τ_s is the shear strength. Eq. (1) defines the Mohr effective stress failure envelope. It can be constructed by touching a set of the Mohr circles, which are obtained from a series of compression and tension tests on core specimens of a soil or rock, and forms a parabolic locus as shown in Fig. 1.

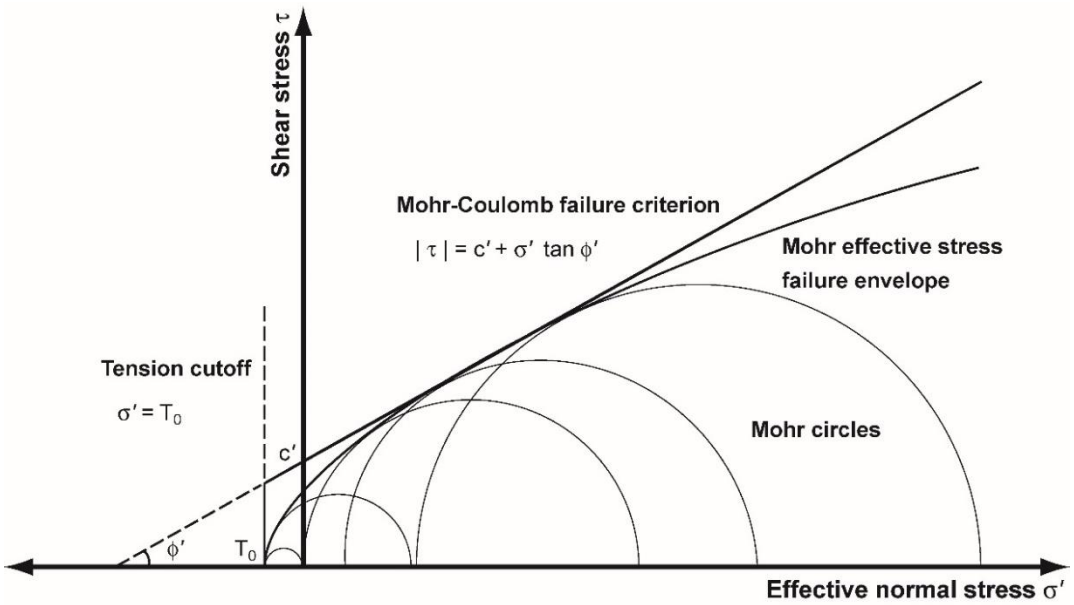

Fig. 1 Schematic diagram of the Mohr effective stress failure envelope approximated by the Mohr-Coulomb failure criterion and the tension cutoff

For saturated-unsaturated soils and rocks, the Mohr effective stress failure envelope can be approximated by the following shear strength equation, i.e., the modified or extended Mohr-Coulomb failure criterion (Mohr 1900, Jaeger and Cook 1979, Das 1994) as shown in Fig. 1:

$$|\tau| = \tau_s = c' + \sigma' \tan \phi' \tag{2}$$

where c' is the effective cohesion or effective shear strength intercept, and ϕ' is the effective angle of internal friction.

The modified Mohr-Coulomb failure criterion (Mohr 1900, Jaeger and Cook 1979, Das 1994), i.e., Eq. (2) implies that the shear failure occurs when the applied shear stress less (minus) the frictional resistance associated with the compressive effective normal stress on a surface is greater than or equal to the effective cohesion; that is, when the corresponding Mohr circle touches or crosses the Mohr-Coulomb failure criterion. However, it is not reasonable to admit a frictional resistance in the presence of a tensile effective normal stress on a failure surface. As a result, Eq. (2) loses its physical validity when the effective normal stress crosses into the tensile region. In order to overcome this problem, the following tension cutoff (Goodman 1989) has also to be superimposed on the Mohr-Coulomb failure criterion as shown in Fig. 1:

$$\sigma' = T_o \tag{3}$$

where T_o is the tensile strength ($T_o \leq 0$). Thus, Eq. (2) is valid only when the minimum principal effective stress σ'_3 is greater than the tensile strength T_o (i.e., $\sigma'_3 > T_o$). As a result, the tension failure occurs instead of the shear failure when the minimum principal effective stress is smaller than or equal to the tensile strength (i.e., $\sigma'_3 \leq T_o$) even though the Mohr circle touches or crosses the Mohr-Coulomb failure criterion, i.e., Eq. (2). In other words, Eqs. (2) and (3) form a bilinear failure criterion for both shear and tension failures.

The factor of safety against shear failure F_s is defined as the ratio of the shear strength to the shear stress acting on a potential failure surface under a given stress condition σ'_1 and σ'_3, and hence it can be expressed from Fig. 2 as follows:

$$F_s = \frac{\overline{AC}}{\overline{AB}} = \frac{\sin\phi'\,(\sigma'_m + c'\cot\phi')}{\tau_{max}} = \frac{\sigma'_m \sin\phi' + c'\cos\phi'}{\tau_{max}} \tag{4}$$

where $\sigma'_m = (\sigma'_1 + \sigma'_3)/2$ is the mean effective normal stress, and $\tau_{max} = (\sigma'_1 - \sigma'_3)/2$ is the maximum shear stress equal to the half of the deviatoric effective stress $\sigma'_d = \sigma'_1 - \sigma'_3 = 2\tau_{max}$. If the factor of safety against shear failure F_s is greater than or equal to unity (i.e., $\tau_{max} \leq \sigma'_m \sin\phi' + c'\cos\phi'$ and thus $1 \leq F_s$), the geologic medium at the corresponding location is considered to be stable with respect to the shear failure. If it is smaller than unity and greater than or equal to zero (i.e., $0 \leq \sigma'_m \sin\phi' + c'\cos\phi' < \tau_{max}$ and thus $0 \leq F_s < 1$), the geologic medium is considered to be unstable with respect to the shear failure. If it is smaller than zero (i.e., $\sigma'_m \sin\phi' + c'\cos\phi' < 0$ and thus $F_s < 0$), the mean effective normal stress crosses into the tensile region, and the geologic medium is considered to be unstable with respect to the tension failure, not the shear failure as described in the above-mentioned bilinear failure criterion (i.e., Eqs. (2) and (3)).

On the other hand, the factor of safety against tension failure F_t is defined as the ratio of the maximum principal effective stress less (minus) the tensile strength to the deviatoric effective stress acting on a potential failure surface under a given stress condition σ'_1 and σ'_3, and hence it can be expressed from Fig. 2 as follows:

$$F_t = \frac{\overline{DF}}{\overline{DE}} = \frac{\sigma'_1 - T_o}{\sigma'_1 - \sigma'_3} = \frac{\sigma'_1 - T_o}{2\tau_{max}} \tag{5}$$

If the factor of safety against tension failure F_t is greater than or equal to unity (i.e., $T_o \leq \sigma'_3 < \sigma'_1$ and thus $1 \leq F_t$), the geologic medium at the corresponding location

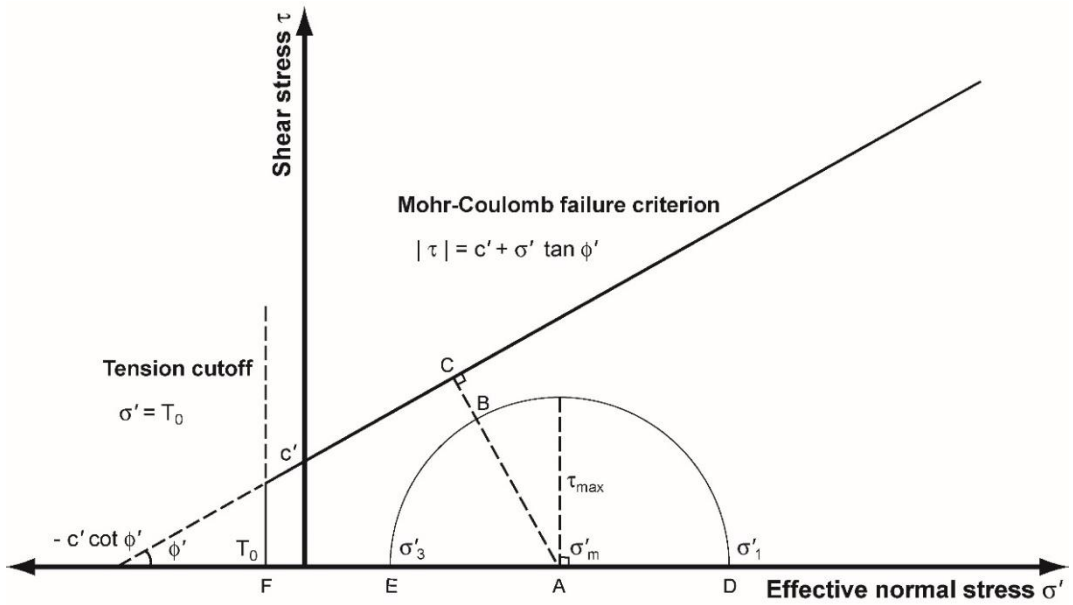

Fig. 2 Schematic diagram of the Mohr circle under the Mohr-Coulomb failure criterion and the tension cutoff for the factors of safety against shear and tension failures

is considered to be stable with respect to the tension failure. If it is smaller than unity and greater than or equal to zero (i.e., $\sigma'_3 < T_o \leq \sigma'_1$ and thus $0 \leq F_t < 1$), the geologic medium is considered to be unstable with respect to the tension failure in the minimum principal plane direction. If it is smaller than zero (i.e., $\sigma'_3 < \sigma'_1 < T_o$ and thus $F_t < 0$), the geologic medium is considered to be unstable with respect to the tension failure in both minimum and maximum principal plane directions.

However, an unstable zone, in which the factor of safety against shear failure F_s is smaller than unity and greater than or equal to zero (i.e., $0 \leq F_s < 1$) using Eq. (4), can often overlap spatially with another unstable zone, in which the factor of safety against tension failure F_t is smaller than unity and greater than or equal to zero (i.e., $0 \leq F_t < 1$) using Eq. (5), because these two equations are derived independently of each other. As a result, by using Eqs. (4) and (5) independently alone, one cannot distinguish a potential shear failure zone from a potential tension failure zone within a geologic medium, and thus rigorous analysis of shear and tension failure potential may be difficult or impossible. Therefore, in order to determine practically which one between the shear and tension failures actually takes place or not as described in the above-mentioned bilinear failure criterion (i.e., Eqs. (2) and (3)), the factors of safety against shear and tension failures F_s and F_t (i.e., Eqs. (4) and (5)) have to be considered dependently together to determine three potential shear and tension failure indices as follows:

$$\begin{aligned}
&\text{If } 1 \leq F_t \ \&\ 1 \leq F_s: && I_s = 0 \ \&\ I_t = 0 \ (I_f = 0)\\
&\text{If } 1 \leq F_t \ \&\ 0 \leq F_s < 1: && I_s = 1 \ \&\ I_t = 0 \ (I_f = 1)\\
&\text{If } 0 \leq F_t < 1: && I_s = 0 \ \&\ I_t = 1 \ (I_f = -1)\\
&\text{If } F_t < 0: && I_s = 0 \ \&\ I_t = 2 \ (I_f = -2)
\end{aligned} \tag{6}$$

where I_s is the potential shear failure index, I_t is the potential tension failure index, and I_f is the potential (shear and tension) failure index.

If the potential shear failure index I_s is equal to unity (i.e., $I_s = 1$), the shear failure may occur at the corresponding location. If it is equal to zero (i.e., $I_s = 0$), the shear failure may not happen there. Similarly, if the potential tension failure index I_t is equal to unity or two (i.e., $I_t = 1$ or $I_t = 2$), the tension failure may occur at the corresponding location. If it is equal to zero (i.e., $I_t = 0$), the tension failure may not happen there. Here both potential shear and tension failure indices I_s and I_t cannot be greater than zero simultaneously at a location (i.e., both shear and tension failure zones do not overlap spatially). Thus, they can also be further combined into the potential failure index I_f alone. If the potential failure index I_f is equal to zero (i.e., $I_f = 0$), neither shear failure nor tension failure may occur at the corresponding location. If it is equal to unity (i.e., $I_f = 1$), the shear failure may happen there. If it is equal to negative unity or two (i.e., $I_f = -1$ or $I_f = -2$), the tension failure may happen there. As a result, by using the five local shear and tension failure variables F_s, F_t, I_s, I_t, and I_f (i.e., Eq. (6) with Eqs. (4) and (5)), one can distinguish a potential shear failure zone from a potential tension failure zone within a geologic medium without spatial overlapping, and thus rigorous analysis of shear and tension failure potential may be easy or possible than by using the conventional factors of safety against shear and tension failures F_s and F_t (i.e., Eqs. (4) and (5)) only.

3. Numerical model and implementation

3.1 Numerical model

The poroelastic hydromechanical numerical model used

in this study is COWADE123D (Kim 1995, 2002, 2006). This numerical model is a generalized multidimensional Galerkin finite element model and can simulate fully coupled groundwater flow and land deformation in saturated-unsaturated geologic media, which are heterogeneous and anisotropic, due to various causes such as pumping, loading, mining, tunneling, rainfall, and others. For more details on the numerical formulations of COWADE123D (Kim 1995, 2002, 2006), the readers are referred to the works of Kim (1996), Kim and Parizek (1999a), and Kim (2003, 2005).

The first version (Kim 1995) of COWADE123D was verified by Kim (1996) and Kim and Parizek (1999a) for its numerical accuracy by comparing numerical solutions with analytical solutions for pressure head (or excessive pore water pressure) and vertical and horizontal (radial) land displacements due to surface loading on a fully saturated column (Biot 1941), groundwater pumping from a fully saturated confined aquifer (Bear and Corapcioglu 1981b), and groundwater pumping from a fully saturated unconfined aquifer (Corapcioglu and Bear 1983). In all the three cases, the numerical solutions showed almost perfect agreement with the analytical solutions.

3.2 Numerical implementation

In COWADE123D (Kim 1995, 2002, 2006), once simultaneous numerical solutions of the pressure head h and displacements u_i for the poroelastic hydromechanical governing equations are obtained at each nonlinear iteration level or time step, the strain tensor ε_{ij} (positive for tension) is calculated from the displacement vector u_i using the displacement-strain relationship, and then the (deformation-producing) effective stress tensor σ'_{ij} (positive for tension) is calculated from the resulting strain tensor ε_{ij} using the generalized Hooke's law for $i,j = x,y,z$ (Love 1944, Lekhnitskii 1963). After the sign reversal of the effective stress tensor for convenience, the maximum, intermediate, and minimum principal effective stresses σ'_1, σ'_2, and σ'_3 (positive for compression) are calculated from the resulting effective stress tensor σ'_{ij} using the multidimensional coordinate transformation (Jaeger and Cook 1979, Goodman 1989). Finally, the above-mentioned five local shear and tension failure variables F_s, F_t, I_s, I_t, and I_f are calculated from the maximum and minimum principal effective stresses σ'_1 and σ'_3, the effective cohesion c', the effective angle of internal friction ϕ', and the tensile strength T_o by using Eqs. (4), (5), and (6).

The following constitutive mathematical equations (Kim and Parizek 1999b) are also adopted in this study to account for the changes in the porosity $n(\varepsilon_{ij})$ and the saturated hydraulic conductivity tensor $K_{sat\ ij}(\varepsilon_{ij})$ by solid skeleton deformation:

$$n = 1 - \frac{1-n^o}{1+\varepsilon_v} \tag{7}$$

$$K_{sat\ ij} = K^o_{sat\ ij}\left[\frac{1}{n^o}(1+\varepsilon_v)^{\frac{2}{3}} - \frac{1-n^o}{n^o}(1+\varepsilon_v)^{-\frac{1}{3}}\right]^3 \tag{8}$$

where $\varepsilon_{ij} = \partial u_i/\partial x_j + \partial u_j/\partial x_i\,(1-\delta_{ij})$ is the strain tensor (positive for tension), $\varepsilon_v = \varepsilon_{xx} + \varepsilon_{yy} + \varepsilon_{zz}$ is the volumetric strain (positive for tension), n^o is the initial porosity prior to deformation, and $K^o_{sat\ ij}$ is the initial saturated hydraulic conductivity tensor prior to deformation for $i,j = x,y,z$. Here u_i is the displacement vector component in the i direction, and δ_{ij} is Kronecker's delta for $i,j = x,y,z$.

4. Numerical simulations: Case studies

4.1 Case 1: Soil slope under rainfall

A variably saturated soil slope under rainfall is considered as Case 1. The slope is a valley-shape excavation slope located in Seoul, Korea. The slope material is composed of silty soil (silt), which was produced by weathering of granite and gneiss bedrock. In Seoul and its surrounding area, rainfall-induced slope failures and landslides have often been reported during and even right after intensive rainfall periods every year in the 1990s. In Seoul, the rainiest month in the 1990s was August with the average monthly rainfall amount of 407 mm, which corresponds to the highest monthly rainfall rate of 1.52×10^{-7} m/s (KMA 1990-1999). Using the above-mentioned hydromechanical numerical model COWADE123D (Kim 1995, 2002, 2006), a steady-state numerical simulation is performed for the variably saturated soil slope under the highest monthly rainfall rate.

As shown in Fig. 3, the cross section of the valley-shape excavation slope (i.e., 100 m × 40 m) is taken as a two-dimensional vertical system (x, z) considering the lateral symmetry with respect to the vertical centerline of the slope at x = 0 m and assuming plane strain in the y direction perpendicular to the cross section. The slope has an inclination of 26.6° (2:1 slope) and a flat foundation with a length of 60 m at the slope crest to consider the laterally infinite domain. The cross section is then discretized into 624 isoparametric quadrilateral elements with 680 nodes.

The following constitutive mathematical equations (van Genuchten 1980) are employed here to consider the changes in the degree of water saturation $S_w(h)$ and the relative hydraulic conductivity $K_r(h)$ by unsaturated water flow for $h < 0$:

$$S_w = S_{wr} + (1-S_{wr})(1+|\alpha_v h|^{n_v})^{-m_v} \tag{9}$$

$$K_r = (1+|\alpha_v h|^{n_v})^{-\frac{m_v}{2}}\left[1 - \left(\frac{|\alpha_v h|^{n_v}}{1+|\alpha_v h|^{n_v}}\right)^{m_v}\right]^2 \tag{10}$$

where h is the pressure head, S_{wr} is the degree of residual water saturation, $\alpha_v = -1/h_a$ and n_v are van Genuchten's unsaturated hydraulic parameters ($\alpha_v > 0$ and $n_v > 1$), h_a is the air-entry (bubbling) pressure head ($h_a < 0$), and $m_v = 1 - 1/n_v$ $(0 < m_v < 1)$.

The silt is assumed to be homogeneous and isotropic, and its material properties are obtained from a series of field and laboratory tests and the literature (Lambe and Whitman 1979, Carsel and Parrish 1988, Das 1994, Bardet 1997) and summarized in Table 1. The compressibility of water β_w,

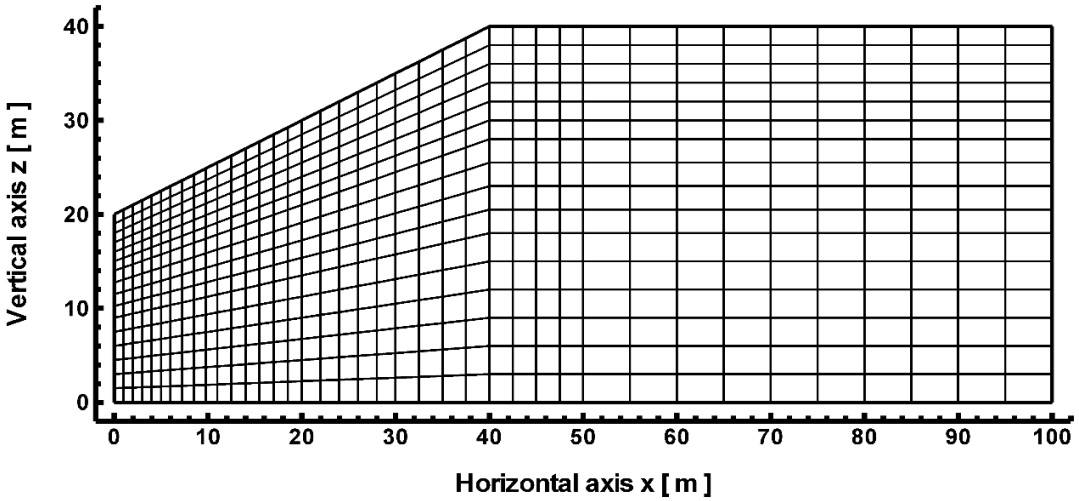

Fig. 3 Schematic diagram of the slope and finite element mesh used in the numerical simulation

Table 1 Material properties of the silt in the slope used in the numerical simulation

Property	Symbol	Value
Initial porosity	n^o	0.46
Initial saturated hydraulic conductivity tensor*	$K^o_{sat\ ij}$	$6.94 \times 10^{-7}\ \delta_{ij}$ m/s
Poisson's ratio*	$\nu = \nu_{ij}$	0.33
Young's modulus*	$E = E_i$	1.10×10^7 N/m^2
Shear modulus*	$G = G_{ij}$	4.14×10^6 N/m^2
Biot's hydromechanical coupling coefficient tensor*	$\alpha_{c\ ij}$	$1.00\ \delta_{ij}$
Solid density	ρ_s	2.67×10^3 kg/m^3
Degree of residual water saturation	S_{wr}	7.39×10^{-2}
van Genuchten's (1980) unsaturated hydraulic parameters	α_v	1.60 m^{-1}
	n_v	1.37
Effective cohesion	c'	1.00×10^4 N/m^2
Effective angle of internal friction	ϕ'	30.00°
Tensile strength	T_o	0.00 N/m^2

*$i, j = x, y, z;\ G = E/[2(1+\nu)];\ \delta_{ij}$ is Kronecker's delta

density of water ρ_w, and gravitational acceleration constant g are set equal to 4.40×10^{-10} m^2/N, 1,000 kg/m^3, and 9.81 m/s^2, respectively (Freeze and Cherry 1979).

Along the left-hand side at x = 0 m, a no-flow boundary condition and a no-horizontal displacement boundary condition are applied, but vertical displacement is allowed considering the lateral symmetry with respect to the vertical centerline of the slope. The same boundary conditions are also applied along the right-hand side at x = 100 m considering the laterally infinite domain. The impermeable bottom surface at z = 0 m is fixed vertically, but it is free to move horizontally considering the unweathered fresh bedrock (hard rock). The top slope surface at 20 m $\leq z \leq$ 40 m is free to move both vertically and horizontally, and it is treated as a permeable solid-air interface by applying a variable rainfall-infiltration-seepage boundary condition (Huyakorn *et al*. 1986, Yeh 1987, 1999) with the above-mentioned highest monthly rainfall rate in order to take into account infiltration and seepage occurring simultaneously along it during rainfall. For such a slope surface, the maximum pressure head h_{max} is set equal to zero in order to prevent water accumulation (ponding) on it.

The steady-state numerical simulation results for the pressure head, hydraulic head, Darcy velocity (groundwater flow flux), and displacement vector are shown in Fig. 4. As shown in Fig. 4(a), the water table, on which the pressure head is equal to zero, is exposed along the slope surface up to 11.47 m high from the slope toe, and thus an unsaturated zone, which is above the water table, is developed only below the slope surface near the slope crest. As shown in Fig. 4(b), the maximum hydraulic head is equal to 39.77 m and located at the slope crest (i.e., x = 40.00 m, z = 40.00 m), and the hydraulic gradient is steepest and concentrated at the slope toe (i.e., x = 0.00 m, z = 20.00 m). As a result, the Darcy velocity increases toward the slope toe, and its maximum is equal to 1.11×10^{-6} m/s at the slope toe as shown in Fig. 4(c). It should also be recognized from Fig. 4(c) that the height of the seepage face is equal to 10.00 m from the slope toe by inspecting the groundwater flow

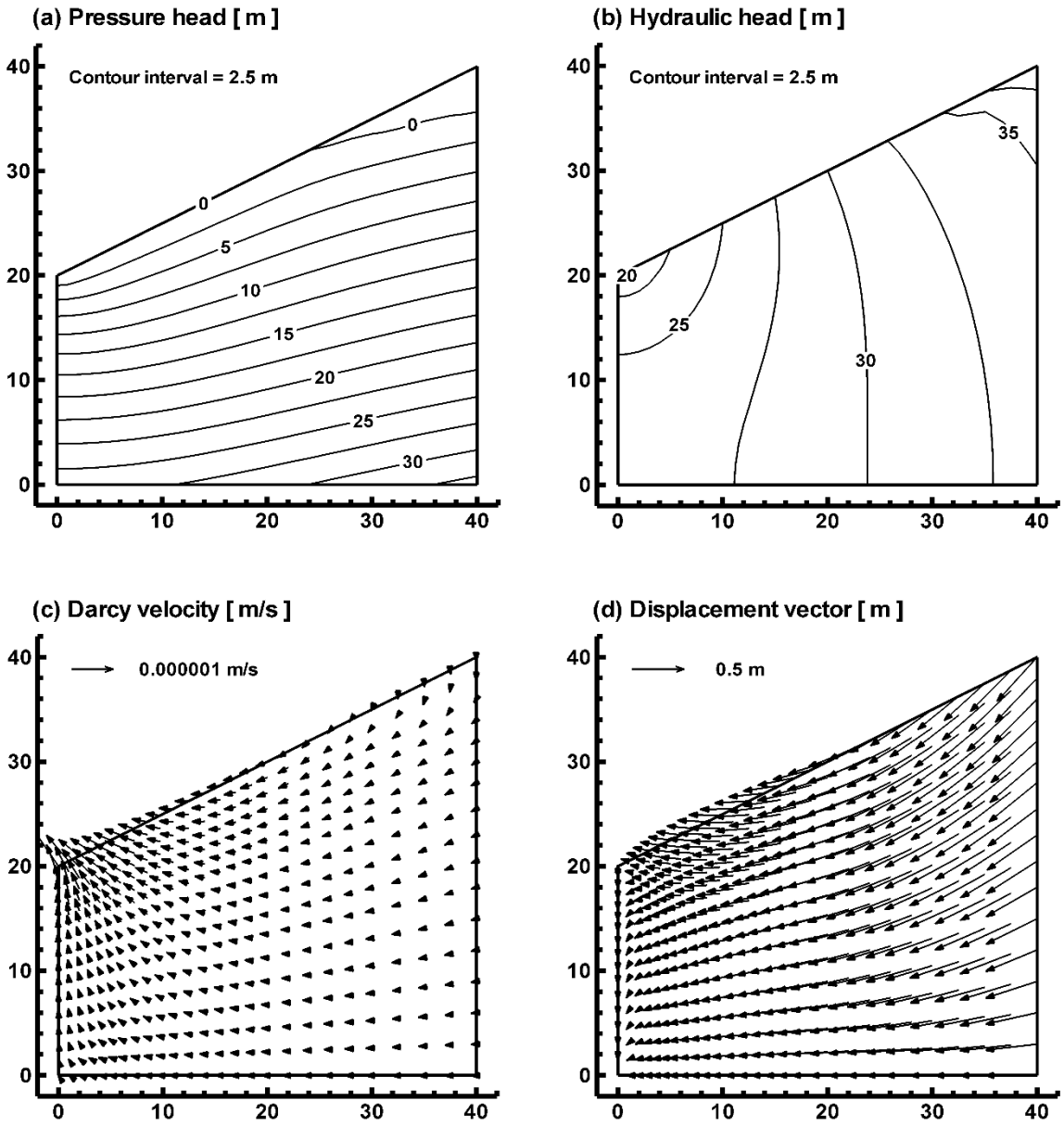

Fig. 4 Steady-state spatial distributions of (a) pressure head, (b) hydraulic head, (c) Darcy velocity (groundwater flow flux), and (d) displacement vector in the slope (The units of the horizontal and vertical coordinate axes are m as shown in Fig. 3.)

direction across the slope surface. A seepage face is defined as a permeable solid-air interface along which the pressure head is equal to zero, and the Darcy velocity is outward from a geologic medium (i.e., slope in this case study). As a result, the rainwater infiltration occurs along the slope surface more than 10.00 m high from the slope toe, while the groundwater seepage takes place along the slope surface less than 10.00 m high from the slope toe, under the rainfall rate. It means that the exposed water table does not coincide spatially with the seepage face under such a high rainfall rate, and thus the rainwater infiltration occurs instead of the groundwater seepage along the remaining part of the exposed water table that excludes the seepage face; that is, along the slope surface between 10.00 m and 11.47 m high from the slope toe. As shown in Fig. 4(d), the displacement vector is downward near the slope crest and upward near the slope toe showing a curved pattern of the overall slope deformation.

The steady-state numerical simulation results for the five local shear and tension failure variables are shown in Fig. 5 (i.e., F_s, I_s, F_t, and I_t) and summarized in Table 2 (i.e., F_s, F_t, I_s, I_t, and I_f). As shown in Fig. 5(a), the unstable zone, in which the factor of safety against shear failure F_s is smaller than unity, becomes thicker near the slope toe and propagates toward the slope crest showing a downward convex shape. The minimum factor of safety against shear failure is equal to 0.54 and located on the slope surface at a height of 2.00 m from the slope toe. However, as shown in Fig. 5(b), the potential shear failure zone, in which the potential shear failure index I_s is equal to unity, is developed only in a part of the unstable zone where the factor of safety against shear failure F_s is

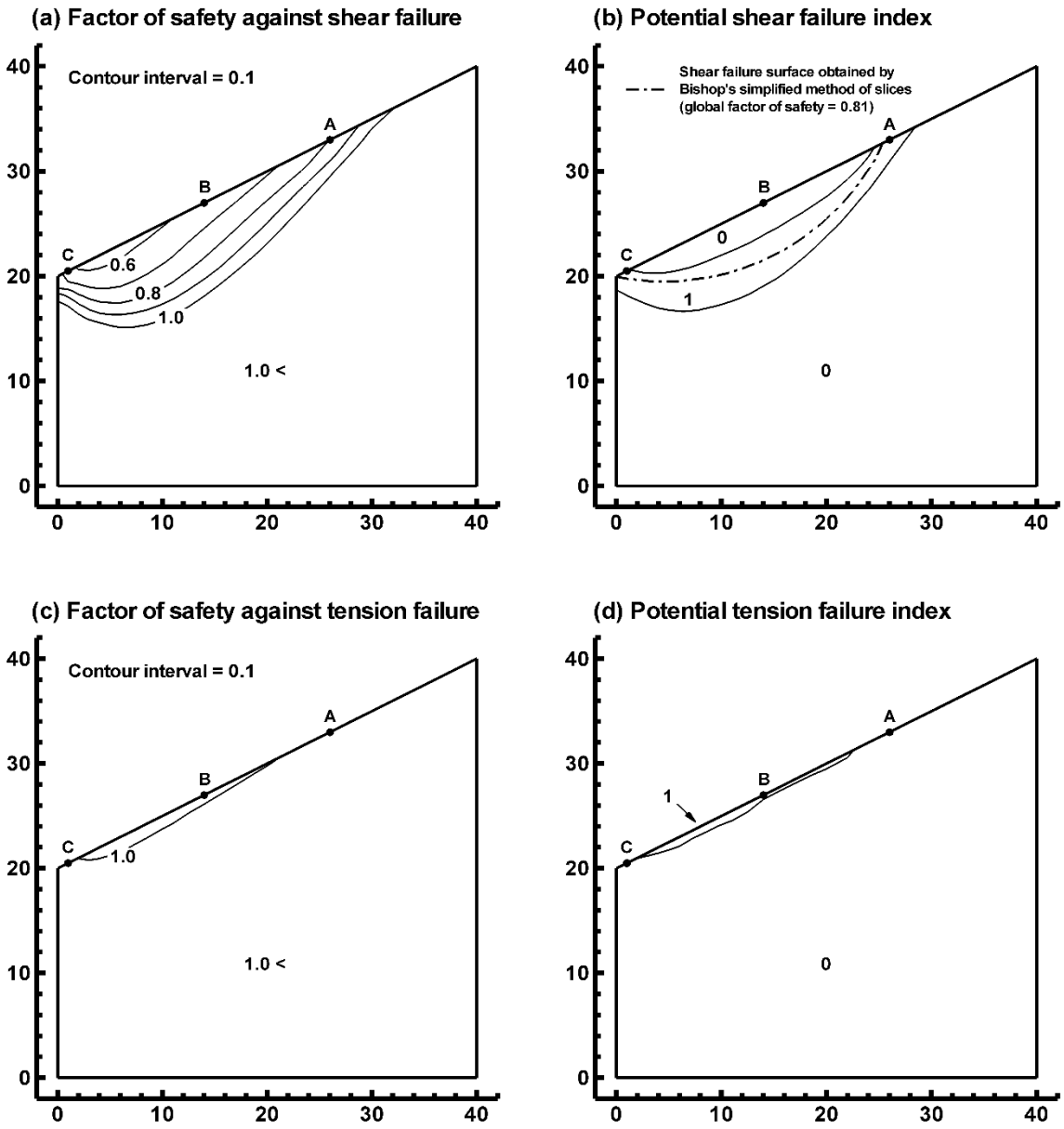

Fig. 5 Steady-state spatial distributions of (a) factor of safety against shear failure, (b) potential shear failure index, (c) factor of safety against tension failure, and (d) potential tension failure index in the slope (The units of the horizontal and vertical coordinate axes are m as shown in Fig. 3.)

Table 2 Local shear and tension failure variables on the slope surface

Point (location)*	Coordinates	F_s	F_t	I_s	I_t	I_f
A (closer to slope crest)	x = 26.00 m, z = 33.00 m	0.80	1.10	1	0	1
B (intermediate)	x = 14.00 m, z = 27.00 m	0.63	0.99	0	1	−1
C (closer to slope toe)	x = 01.00 m, z = 20.50 m	0.66	1.12	1	0	1

*The three points A, B, and C are marked in Fig. 5

smaller than unity and greater than or equal to 0.66 showing a curved shape from the slope toe toward the slope crest (Table 2). Such a potential shear failure zone is very well matched with a circular shear failure surface obtained by Bishop's simplified method of slices (Das 1994, Huang 2014), which is a limit equilibrium method (Fig. 5(b)). In the remaining part of the unstable zone where the factor of safety against shear failure F_s is smaller than 0.66, the factor of safety against tension failure F_t is slightly smaller than unity as shown in Fig. 5(c), and the potential tension failure index I_t is equal to unity as shown in Fig. 5(d). This strongly suggests that the tension failure is likely to occur instead of the shear failure in the remaining part of the unstable zone between the potential shear failure zone

and the slope surface since the minimum principal effective stress σ'_3 is in a tensional state and slightly smaller than the tensile strength there. However, the minimum factor of safety against tension failure is equal to 0.98 and located on the slope surface at a height of 2.50 m from the slope toe as shown in Fig. 5(c), and the potential tension failure zone, in which the potential tension failure index I_t is equal to unity, is very thin along the slope surface as shown in Fig. 5(d) compared with the potential shear failure zone (Fig. 5(b)). These indicate that the tension failure near the slope surface may not be as severe as the shear failure in the slope (Table 2). As a result, the potential tension failure zone, in which the potential tension failure index I_t is equal to two, is not developed near the slope surface as shown in Fig. 5(d) since only the minimum principal effective stress σ'_3 is smaller than the tensile strength there. It should also be recognized that the potential tension failure zone delineated in Fig. 5(d) does not overlap spatially with the potential shear failure zone delineated in Fig. 5(b). However, the unstable zone with respect to the tension failure illustrated in Fig. 5(c) overlaps spatially with the unstable zone with respect to the shear failure illustrated in Fig. 5(a). These strongly suggest that shear and tension failure potential and stability of the variably saturated geologic medium associated with the slope can be better analyzed by using the five local shear and tension failure variables as a set than by using the conventional factors of safety against shear and tension failures only.

4.2 Case 2: Weathered rock under tunneling

Tunneling of a subway before reinforcement and lining is considered as Case 2. The subway is Subway Line 2 located in Busan, Korea. Construction of its first phase was initiated in November 1991 and completed in June 1999, and the other phases have been constructed later. The first-phase tunnel was mainly constructed through weathered granite bedrock (soft rock), which was classified as a poor rock (Class IV) with the rock mass rating (RMR) of 37 (Lee and Kim 1999). Prior to the start of tunneling, the average annual regional water table depth was about 3.24 m from the ground surface (BUTA 1992). The average annual rainfall amount in Busan during the first-phase tunneling period was about 1,505 mm, which corresponds to the average annual rainfall rate of 4.77×10^{-8} m/s (KMA 1991-1999). The initial (pretunneling) horizontal stress coefficient $K^o = \sigma_h^o / \sigma_v^o$ in the first-phase area was determined to be about 0.50 (Lee and Kim 1999). Here σ_h^o is the initial horizontal total normal stress, and σ_v^o is the initial vertical total normal stress. Using the above-mentioned hydromechanical numerical model COWADE-123D (Kim 1995, 2002, 2006), a transient-state numerical simulation is performed for the variably saturated weathered rock under tunneling.

As shown in Fig. 6, the cross section of the weathered rock around the tunnel (i.e., 100 m × 50 m) is taken as a two-dimensional vertical system (x, z) considering the lateral symmetry with respect to the vertical centerline of the tunnel at x = 0 m and assuming plane strain in the y direction perpendicular to the cross section. The tunnel is at an average depth of 13.30 m below the ground surface and has a horseshoe shape with a height of 8.44 m and a width of 10.54 m to disperse stress around the tunnel (BUTA 1992). The cross section is then discretized into 440 isoparametric quadrilateral elements with 490 nodes.

The following constitutive mathematical equations (Huyakorn *et al*. 1984) are employed here to consider the changes in the degree of water saturation $S_w(h)$ and the relative hydraulic conductivity $K_r(h)$ by unsaturated water flow for $h_b < h < h_a$:

$$S_w = 1 - (1 - S_{wr}) \frac{h - h_a}{h_b - h_a} \tag{11}$$

$$K_r = \left[1 - (1 - S_{wr}) \frac{h - h_a}{h_b - h_a} - S_{wr}\right] (1 - S_{wr})^{-1} \tag{12}$$

where h is the pressure head, S_{wr} is the degree of residual water saturation, h_a is the air-entry (bubbling) pressure head ($h_a \leq 0$), and h_b is the allowed minimum pressure head ($h_b < h_a$).

The weathered granite is assumed to be homogeneous and isotropic, and its material properties are obtained from a series of field and laboratory tests and the literature (Lee and Park 1976, Goodman 1989, BUTA 1992, Lee and Kim 1999) and summarized in Table 3. The compressibility of water β_w, density of water ρ_w, and gravitational acceleration constant g are set equal to 4.40×10^{-10} m^2/N, 1,000 kg/m^3, and 9.81 m/s^2, respectively (Freeze and Cherry 1979).

Prior to the start of tunneling, the system is assumed to be at a hydrostatic equilibrium condition corresponding to the above-mentioned average annual regional water table depth; that is, the pretunneling (initial) hydraulic head is equal to 46.76 m everywhere from the bottom surface at z = 0 m. The initial shear stress is set equal to zero since both isotropic geologic medium (weathered granite) and no far-field or tectonic stress are assumed in this case study.

Along the left-hand side at x = 0 m, a no-flow boundary condition and a no-horizontal displacement boundary condition are applied, but vertical displacement is allowed considering the lateral symmetry with respect to the vertical centerline of the tunnel. Along the right-hand side at x = 100 m, a constant hydraulic head boundary condition with its pretunneling value (i.e., 46.76 m) and a no-horizontal displacement boundary condition are applied, but vertical displacement is allowed considering the laterally infinite domain. The impermeable bottom surface at z = 0 m is fixed vertically, but it is free to move horizontally considering the unweathered fresh bedrock (hard rock). The top ground surface at z = 50 m is free to move both vertically and horizontally, and it is treated as a permeable solid-air interface by applying a variable rainfall-infiltration boundary condition (Huyakorn *et al*. 1986, Yeh 1987, 1999) with the above-mentioned average annual rainfall rate in order to take into account possible spatial changes in the infiltration rate along it during tunneling. For such a ground surface, the maximum pressure head h_{max} is set equal to its pretunneling value (i.e., -3.24 m) in order to prevent an undesirable water table rise over its pretunneling depth up to the ground surface because it is not likely to happen during tunneling in most real situations. On the other hand,

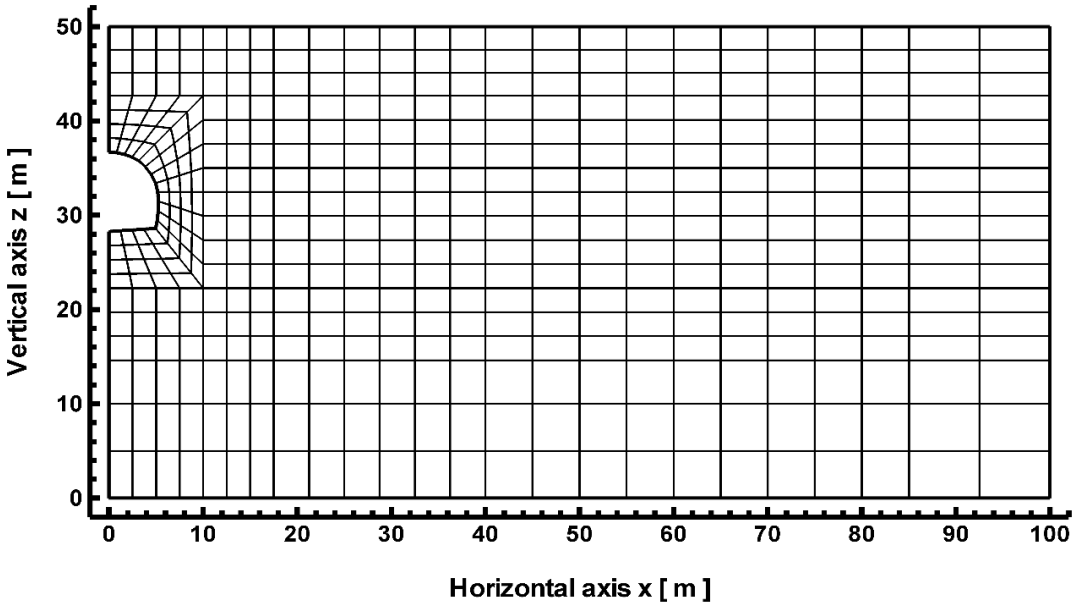

Fig. 6 Schematic diagram of the tunnel and finite element mesh used in the numerical simulation

Table 3 Material properties of the weathered granite around the tunnel used in the numerical simulation

Property	Symbol	Value
Initial porosity	n^o	0.17
Initial saturated hydraulic conductivity tensor*	$K^o_{sat\ ij}$	$1.81 \times 10^{-6}\ \delta_{ij}$ m/s
Poisson's ratio*	$\nu = \nu_{ij}$	0.30
Young's modulus*	$E = E_i$	1.96×10^8 N/m^2
Shear modulus*	$G = G_{ij}$	7.54×10^7 N/m^2
Biot's hydromechanical coupling coefficient tensor*	$\alpha_{c\ ij}$	$1.00\ \delta_{ij}$
Solid density	ρ_s	2.66×10^3 kg/m^3
Degree of residual water saturation	S_{wr}	1.00×10^{-1}
Huyakorn *et al.*'s (1984) unsaturated hydraulic parameters	h_a	-0.50 m
	h_b	-25.00 m
Effective cohesion	c'	4.90×10^4 N/m^2
Effective angle of internal friction	ϕ'	35.00°
Tensile strength	T_o	-1.88×10^4 N/m^2

*$i, j = x, y, z;\ G = E/[2(1+\nu)];\ \delta_{ij}$ is Kronecker's delta

the tunnel surface at 28.26 m $\leq z \leq$ 36.70 m is free to move both vertically and horizontally by applying a surface traction boundary condition under the overburden load (gravitational body force) and the above-mentioned pretunneling horizontal stress coefficient, and it is treated as a permeable solid-air interface by applying a variable seepage boundary condition (Huyakorn *et al*. 1986, Yeh 1987, 1999) in order to account for seepage and desaturation occurring simultaneously along it during tunneling. For such a tunnel surface, the maximum pressure head h_{max} is set equal to zero in order to prevent water accumulation (ponding) on it, and no water flow is allowed into the surrounding geologic medium from the tunnel.

The final steady-state numerical simulation results for the pressure head, hydraulic head, Darcy velocity (groundwater flow flux), and displacement vector are shown in Fig. 7. It takes about 31 days to arrive at the final steady-state conditions after the start of tunneling. As shown in Fig. 7(a), the water table, which was initially located 3.24 m below the ground surface, declines, and hence the unsaturated zone, which is above the water table, expands downward to the sidewall of the tunnel. As a result, the crown of the tunnel becomes unsaturated, while a seepage face is developed along the sidewall and invert of the tunnel. The minimum pressure head on the tunnel surface is equal to -2.43 m and located at the uppermost part of the crown (i.e., x = 0.00 m, z = 36.70 m), while the minimum pressure head on the ground surface is equal to -14.88 m and located right above the uppermost part of the crown (i.e., x = 0.00 m, z = 50.00 m). As shown in Fig. 7(b), the minimum hydraulic head is equal to 28.26 m and located at the lowermost part of the invert (i.e., x = 0.00 m, z = 28.26 m), and the hydraulic gradient is steepest and concentrated at the lower part of the sidewall (i.e., x =

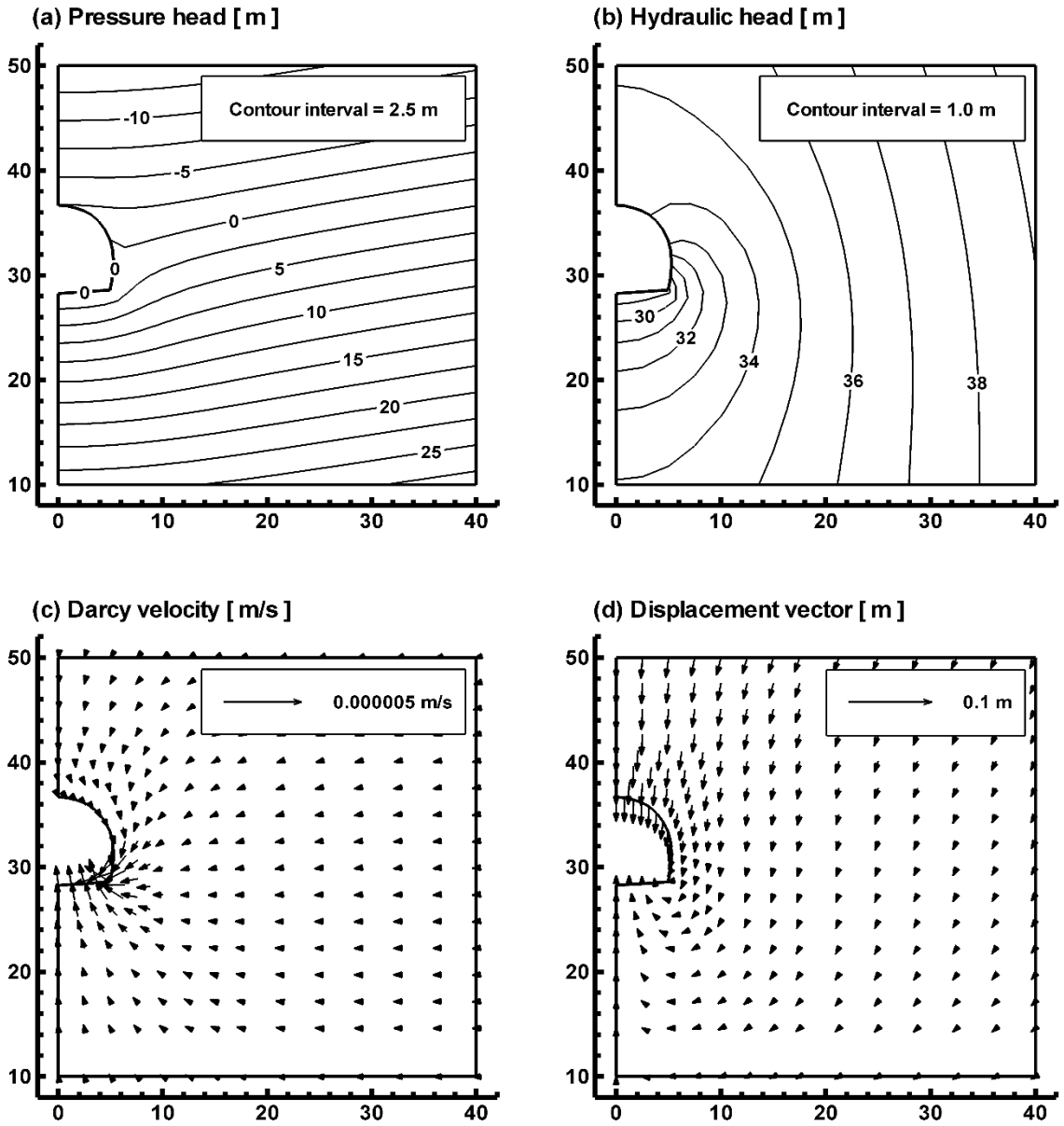

Fig. 7 Final steady-state spatial distributions of (a) pressure head, (b) hydraulic head, (c) Darcy velocity (groundwater flow flux), and (d) displacement vector around the tunnel (The units of the horizontal and vertical coordinate axes are m as shown in Fig. 6.)

5.24 m, z = 30.45 m). As a result, the Darcy velocity increases toward the lower part of the sidewall and then the invert, and its maximum is equal to 2.08 × 10^{-6} m/s at the lower part of the sidewall as shown in Fig. 7(c). It should also be recognized from Fig. 7(c) that the groundwater does not flow across the tunnel surface but along it at the crown (unsaturated zone), while the groundwater flows across the tunnel surface at the sidewall and invert (seepage face). However, the groundwater also flows across the tunnel surface at the crown during tunneling until it becomes unsaturated. Such similar patterns have been observed during and after tunneling in the actual fields including the study area. As shown in Fig. 7(d), the displacement vector is toward the tunnel surface. As a result, the invert heaves up to 1.20 cm, while the crown subsides down to 2.94 cm. The maximum subsidence on the ground surface occurs right above the uppermost part of the crown and is equal to 2.52 cm indicating the weathered rock between the ground surface and the crown is in a vertically tensional state during tunneling.

The final steady-state numerical simulation results for the five local shear and tension failure variables are shown in Fig. 8 (i.e., F_s, I_s, F_t, and I_t) and summarized in Table 4 (i.e., F_s, F_t, I_s, I_t, and I_f). As shown in Fig. 8(a), the factor of safety against shear failure F_s decreases toward the tunnel surface, and its minimum is equal to 0.13 at the crown, 0.82 at the sidewall, and -0.62 at the invert, respectively (Table 4). However, as shown in Fig. 8(b), the potential shear failure zone, in which the potential shear failure index I_s is equal to unity, is developed only at the lower part of the sidewall showing an ear shape, but it is not observed at the crown and invert where the potential

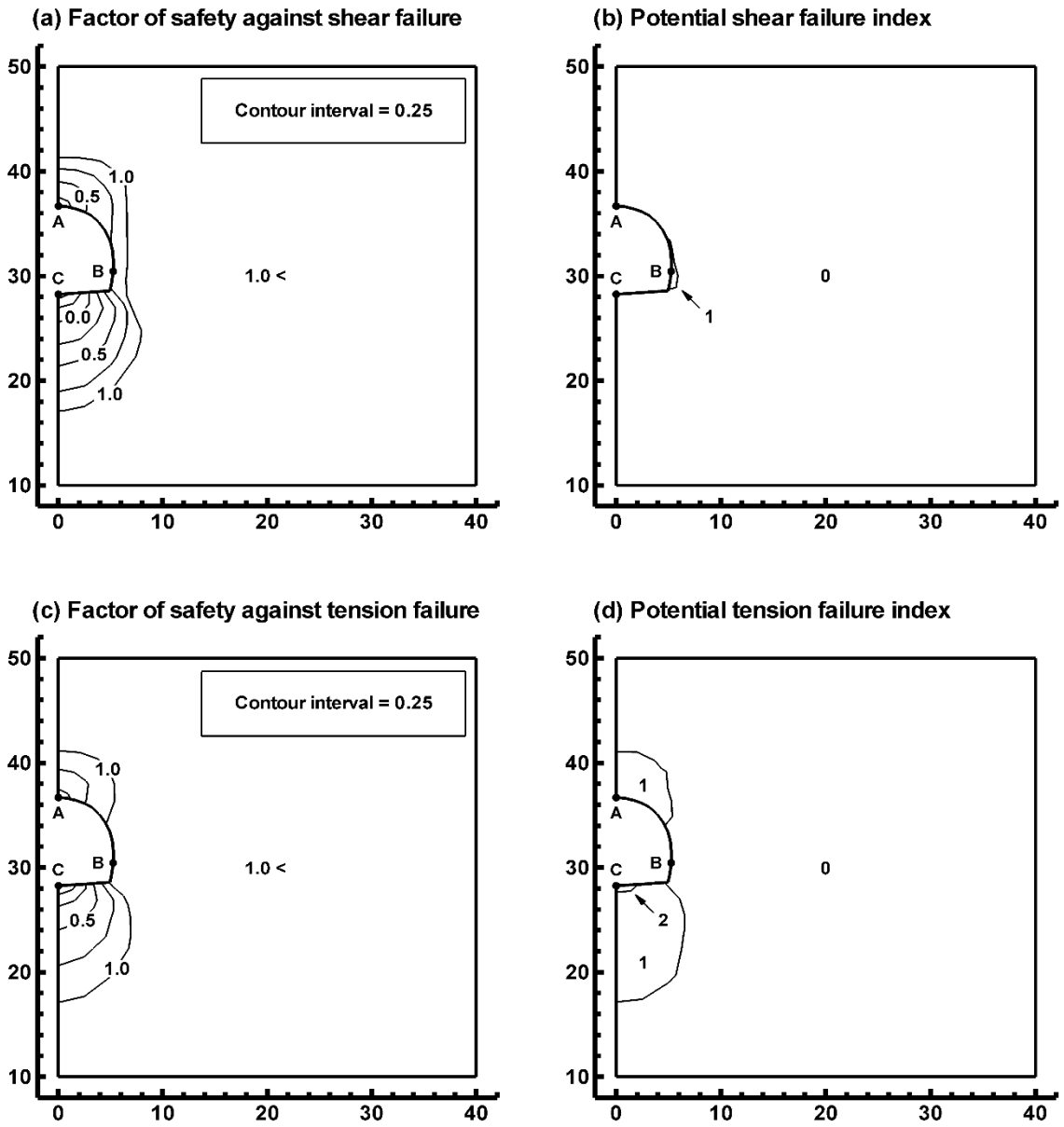

Fig. 8 Final steady-state spatial distributions of (a) factor of safety against shear failure, (b) potential shear failure index, (c) factor of safety against tension failure, and (d) potential tension failure index around the tunnel (The units of the horizontal and vertical coordinate axes are m as shown in Fig. 6.)

Table 4 Local shear and tension failure variables on the tunnel surface

Point (location)*	Coordinates	F_s	F_t	I_s	I_t	I_f
A (uppermost part of crown)	x = 0.00 m, z = 36.70 m	0.13	0.40	0	1	−1
B (lower part of sidewall)	x = 5.24 m, z = 30.45 m	0.82	1.33	1	0	1
C (lowermost part of invert)	x = 0.00 m, z = 28.26 m	−0.62	−0.23	0	2	−2

*The three points A, B, and C are marked in Fig. 8

shear failure index I_s is equal to zero. This strongly suggests that the tension failure is likely to occur instead of the shear failure along the crown and invert since the minimum principal effective stress σ'_3 or both maximum and minimum principal effective stresses σ'_1 and σ'_3 are in tensional states and smaller than the tensile strength there. As shown in Fig. 8(c), the factor of safety against tension failure F_t also decreases toward the tunnel surface, and its minimum is equal to 0.40 at the crown, 1.13 at the sidewall, and -0.23 at the invert, respectively (Table 4). It means that both maximum and minimum principal effective stresses σ'_1 and σ'_3 are smaller than the tensile strength at the invert, while only the minimum principal effective stress σ'_3 is smaller than the tensile strength at the crown. As a result, the potential tension failure index I_t increases toward the invert and the crown, and its value is equal to

two at the invert and unity at the crown, respectively, as shown in Fig. 8(d). These indicate that the tension failure may be more severe at the invert than at the crown (Table 4). As a result, the potential tension failure zone, in which the potential tension failure index I_t is equal to two, is developed at the invert. On the other hand, the potential tension failure index I_t is equal to zero at the sidewall indicating that the tension failure is not likely to occur there. It should also be recognized that the potential tension failure zone delineated in Fig. 8(d) does not overlap spatially with the potential shear failure zone delineated in Fig. 8(b). However, the unstable zone with respect to the tension failure illustrated in Fig. 8(c) overlaps spatially with the unstable zone with respect to the shear failure illustrated in Fig. 8(a). These strongly suggest that shear and tension failure potential and stability of the variably saturated geologic medium associated with the tunnel can be better analyzed by using the five local shear and tension failure variables as a set than by using the conventional factors of safety against shear and tension failures only.

5. Conclusions

A set of relatively simple five local shear and tension failure variables was presented to analyze failure potential and stability of variably saturated geologic media. They are the factor of safety against shear failure F_s, the factor of safety against tension failure F_t, the potential shear failure index I_s, the potential tension failure index I_t, and the potential (shear and tension) failure index I_f. The factor of safety against shear failure F_s was formulated using the geometrical relationship between the Mohr circle and the Mohr-Coulomb failure criterion (effective cohesion and effective angle of internal friction). The factor of safety against tension failure F_t was formulated using the geometrical relationship between the Mohr circle and the tension cutoff (tensile strength). The three potential shear and tension failure indices I_s, I_t, and I_f were then determined considering the factors of safety against shear and tension failures F_s and F_t dependently together. These five local shear and tension failure variables were then implemented into a generalized poroelastic hydro-mechanical numerical model, which is also capable of simulating both unsaturated water flow and rainfall-infiltration-seepage processes on permeable solid-air interfaces such as ground, slope, and tunnel surfaces. Finally, fully coupled groundwater flow and land deformation in two variably saturated geologic media, which are associated with a slope (Case 1) and a tunnel (Case 2), respectively, and their failure potential and stability were simulated using the resultant hydro-mechanical numerical model. The numerical simulation results of both cases show that shear and tension failure potential and stability of variably saturated geologic media can be analyzed numerically simply and efficiently and even better by using the five local shear and tension failure variables as a set than by using the conventional factors of safety against shear and tension failures only. Therefore, it may be concluded that the five local shear and tension failure variables have to be properly utilized together if more rigorous predictions of failure potential and stability of variably saturated geologic media associated with slopes and tunnels are to be obtained.

Acknowledgments

This work was mainly supported by the National Research Foundation (NRF), Ministry of Science and Information and Communications Technology (MSIT), Korea under grant no. 2014-015-C00594. This work was also supported by the Seoul National University Foundation (SNUF), Seoul National University (SNU), Korea under grant no. 2013-3-11. Sungho Lee and Jai-Yong Park were supported in part by the Brain Korea 21 Project funded by the National Research Foundation (NRF), Ministry of Science and Information and Communications Technology (MSIT), Korea. The authors would like to thank the Editor-in-Chief Professor Gye-Chun Cho at the Korea Advanced Institute of Science and Technology (KAIST) for handling this paper and the two anonymous reviewers for their invaluable and constructive review comments on this paper.

References

Ardeshiri-Lajimi, S., Yazdani, M. and Assadi-Langroudi, A. (2016), "A study on the liquefaction risk in seismic design of foundations", *Geomech. Eng.*, **11**(6), 805-820. https://doi.org/10.12989/gae.2016.11.6.805.

Bai, M. and Elsworth, D. (1991), "Modeling subsidence and groundwater flow due to underground mining", *Proceedings of the 34th Annual Meeting of the Association of Engineering Geologists*, Chicago, Illinois, U.S.A., September-October, 981-990.

Bai, M. and Elsworth, D. (1994), "Modeling of subsidence and stress-dependent hydraulic conductivity for intact and fractured porous media", *Rock Mech. Rock Eng.*, **27**(4), 209-234. https://doi.org/10.1007/BF01020200.

Balaban, E. and Onur, M.I. (2018), "Comparison of behaviour of basal reinforced piled embankment with two layer of reinforcement", *Geomech. Eng.*, **16**(3), 233-245. https://doi.org/10.12989/gae.2018.16.3.233.

Bardet, J.P. (1997), *Experimental Soil Mechanics*, Prentice-Hall, Upper Saddle River, New Jersey, U.S.A.

Bear, J. and Corapcioglu, M.Y. (1981a), "Centrifugal filtration in deformable porous media", in Bear, J. and Corapcioglu, M.Y. (Editors), "A series of four papers on water flow in deformable porous media", Technical Report No. UMR-0284, Department of Civil Engineering, University of Michigan, Ann Arbor, Michigan, U.S.A., Section I, 1-42.

Bear, J. and Corapcioglu, M.Y. (1981b), "Mathematical model for regional land subsidence due to pumping, 2. Integrated aquifer subsidence equations for vertical and horizontal displacements", *Water Resour. Res.*, **17**(4), 947-958. https://doi.org/10.1029/WR017i004p00947.

Biot, M.A. (1941), "General theory of three-dimensional consolidation", *J. Appl. Phys.*, **12**(2), 155-164. https://doi.org/10.1063/1.1712886.

Bishop, A.W. and Blight, G.E. (1963), "Some aspects of effective stress in saturated and partly saturated soils", *Géotechnique*, **13**(3), 177-197. https://doi.org/10.1680/geot.1963.13.3.177.

BUTA (1992), "Summary report for enforcement design service of the construction phase 1 of the Busan Subway Line 2", Technical Report No. BUTA-1992-7, Busan Urban Transit

Authority (BUTA), Busan, Korea (in Korean).
Carroll, M.M. (1979), "An effective stress law for anisotropic elastic deformation", *J. Geophys. Res. Solid Earth*, **84**(B13), 7510-7512. https://doi.org/10.1029/JB084iB13p07510.
Carsel, R.F. and Parrish, R.S. (1988), "Developing joint probability distributions of soil water retention characteristics", *Water Resour. Res.*, **24**(5), 755-769. https://doi.org/10.1029/WR024i005p00755.
Cheng, A.H.D. (1997), "Material coefficients of anisotropic poroelasticity", *Int. J. Rock Mech. Min. Sci.*, **34**(2), 199-205. https://doi.org/10.1016/S0148-9062(96)00055-1.
Christian, J.T., Boehmer, J.W. and Martin, P.P. (1972), "Consolidation of a layer under a strip load", *J. Soil Mech. Found. Div.*, *Proc. Am. Soc. Civ. Eng.*, **98**(SM7), 693-707.
Corapcioglu, M.Y. and Bear, J. (1983), "A mathematical model for regional land subsidence due to pumping, 3. Integrated equations for a phreatic aquifer", *Water Resour. Res.*, **19**(4), 895-908. https://doi.org/10.1029/WR019i004p00895.
Coulomb, C.A. (1776), "Essai sur une application des règles de maximis & minimis à quelques problèmes de statique, relatifs à l'architecture", *Mèmoires de Mathématique et de Physique*, **7**, 343-382 (in French).
Cui, L., Cheng, A.H.D., Kaliakin, V.N., Abousleiman, Y. and Roegiers, J.C. (1996), "Finite element analysis of anisotropic poroelasticity: A generalized Mandel's problem and an inclined borehole problem", *Int. J. Numer. Anal. Meth. Geomech.*, **20**(6), 381-401. https://doi.org/10.1002/(SICI)1096-9853(199606)20:6<381::AID-NAG826>3.0.CO;2-Y.
Das, B.M. (1994), *Principles of Geotechnical Engineering*, 3rd Edition, PWS Publishing Company, Boston, Massachusetts, U.S.A.
Freeze, R.A. and Cherry, J.A. (1979), *Groundwater*, Prentice-Hall, Englewood Cliffs, New Jersey, U.S.A.
Ghaboussi, J. and Wilson, E.L. (1973), "Flow of compressible fluid in porous elastic media", *Int. J. Numer. Meth. Eng.*, **5**(3), 419-442. https://doi.org/10.1002/nme.1620050311.
Girrens, S.P., Anderson, C.A., Bennett, J.G. and Kramer, M. (1981), "Numerical prediction of subsidence with coupled geomechanical-hydrological modeling", *Proceedings of the Workshop on Surface Subsidence Due to Underground Mining*, Morgantown, West Virginia, U.S.A., November-December, 63-70.
Goodman, R.E. (1989), *Introduction to Rock Mechanics*, 2nd Edition, John Wiley and Sons, New York, New York, U.S.A.
Huang, Y.H. (2014), *Slope Stability Analysis by the Limit Equilibrium Method: Fundamentals and Methods*, American Society of Civil Engineers Press, Reston, Virginia, U.S.A.
Huyakorn, P.S., Springer, E.P., Guvanasen, V. and Wadsworth, T.D. (1986), "A three-dimensional finite-element model for simulating water flow in variably saturated porous media", *Water Resour. Res.*, **22**(13), 1790-1808. https://doi.org/10.1029/WR022i013p01790.
Huyakorn, P.S., Thomas, S.D. and Thompson, B.M. (1984), "Techniques for making finite elements competitive in modeling flow in variably saturated porous media", *Water Resour. Res.*, **20**(8), 1099-1115. https://doi.org/10.1029/WR020i008p01099.
Jaeger, J.C. and Cook, N.G.W. (1979), *Fundamentals of Rock Mechanics*, 3rd Edition, Chapman and Hall, London, U.K.
Khezri, N., Mohamad, H. and Fatahi, B. (2016), "Stability assessment of tunnel face in a layered soil using upper bound theorem of limit analysis", *Geomech. Eng.*, **11**(4), 471-492. https://doi.org/10.12989/gae.2016.11.4.471.
Kim, J.M. (1995), "COWADE123D: A finite element model for fully coupled saturated-unsaturated water flow in deforming one-, two-, and three-dimensional porous and fractured media, version 1.0", Technical Report No. HGL-1995-9, Hydrogeology Laboratory, Department of Geosciences, Pennsylvania State University, University Park, Pennsylvania, U.S.A.
Kim, J.M. (1996), "A fully coupled model for saturated-unsaturated fluid flow in deformable porous and fractured media", Ph.D. Dissertation, Department of Geosciences, Pennsylvania State University, University Park, Pennsylvania, U.S.A.
Kim, J.M. (2000), "A fully coupled finite element analysis of water-table fluctuation and land deformation in partially saturated soils due to surface loading", *Int. J. Numer. Meth. Eng.*, **49**(9), 1101-1119 https://doi.org/10.1002/1097-0207(20001130)49:9<1101::AID-NME1>3.0.CO;2-K.
Kim, J.M. (2002), "COWADE123D: A finite element model for fully coupled saturated-unsaturated water flow in deforming one-, two-, and three-dimensional porous and fractured media, version 2.11", Technical Report No. GGEL-2002-9, Geological and Groundwater Engineering Laboratory, School of Earth and Environmental Sciences, Seoul National University, Seoul, Korea.
Kim, J.M. (2003), "Integrated modeling for water level fluctuation and land deformation due to groundwater pumping", Final Report No. 5-3-1, Geological and Groundwater Engineering Laboratory, School of Earth and Environmental Sciences, Seoul National University, Seoul, Korea (in Korean with English summary).
Kim, J.M. (2004), "Fully coupled poroelastic governing equations for groundwater flow and solid skeleton deformation in variably saturated true anisotropic porous geologic media", *Geosci. J.*, **8**(3), 291-300. https://doi.org/10.1007/BF02910248.
Kim, J.M. (2005), "Three-dimensional numerical simulation of fully coupled groundwater flow and land deformation in unsaturated true anisotropic aquifers due to groundwater pumping", *Water Resour. Res.*, **41**(1), W01003. https://doi.org/10.1029/2003WR002941.
Kim, J.M. (2006), "COWADE123D: A finite element model for fully coupled saturated-unsaturated water flow in deforming one-, two-, and three-dimensional true anisotropic porous, fractured, and fractured porous geologic media, version 2.17", Technical Report No. GGEL-2006-11, Geological and Groundwater Engineering Laboratory, School of Earth and Environmental Sciences, Seoul National University, Seoul, Korea.
Kim, J.M. and Parizek, R.R. (1997), "Numerical simulation of the Noordbergum effect resulting from groundwater pumping in a layered aquifer system", *J. Hydrol.*, **202**(1-4), 231-243. https://doi.org/10.1016/S0022-1694(97)00067-X.
Kim, J.M. and Parizek, R.R. (1999a), "Three-dimensional finite element modelling for consolidation due to groundwater withdrawal in a desaturating anisotropic aquifer system", *Int. J. Numer. Anal. Meth. Geomech.*, **23**(6), 549-571. https://doi.org/10.1002/(SICI)1096-9853(199905)23:6<549::AID-NAG983>3.0.CO;2-Y.
Kim, J.M. and Parizek, R.R. (1999b), "A mathematical model for the hydraulic properties of deforming porous media", *Ground Water*, **37**(4), 546-554. https://doi.org/10.1111/j.1745-6584.1999.tb01141.x.
Kim, J.M. and Parizek, R.R. (2005), "Numerical simulation of the Rhade effect in layered aquifer systems due to groundwater pumping shutoff", *Adv. Water Resour.*, **28**(6), 627-642. https://doi.org/10.1016/j.advwatres.2004.12.005.
Kim, J.M., Parizek, R.R. and Elsworth, D. (1997), "Evaluation of fully-coupled strata deformation and groundwater flow in response to longwall mining", *Int. J. Rock Mech. Min. Sci.*, **34**(8), 1187-1199. https://doi.org/10.1016/S1365-1609(97)80070-6.
Kim, Y. and Jeong, S. (2017), "Modeling of shallow landslides in

an unsaturated soil slope using a coupled model", *Geomech. Eng.*, **13**(2), 353-370. https://doi.org/10.12989/gae.2017.13.2.353.

KMA (1990-1999), Climatological Data of Seoul for 1990~1999, Korea Meteorological Administration (KMA), Seoul, Korea. <http://www.kma.go.kr>.

KMA (1991-1999), Climatological Data of Busan for 1991~1999, Korea Meteorological Administration (KMA), Seoul, Korea. <http://www.kma.go.kr>.

Lambe, T.W. and Whitman, R.V. (1979), *Soil Mechanics*, *SI Version*, John Wiley and Sons, New York, New York, U.S.A.

Lee, C.J., Jeon, Y.J., Kim, S.H. and Park, I.J. (2016), "The influence of tunnelling on the behaviour of pre-existing piled foundations in weathered soil", *Geomech. Eng.*, **11**(4), 553-570. https://doi.org/10.12989/gae.2016.11.4.553.

Lee, C.Z. and Park, H.I. (1976), "A petrologic study on the acidic igneous rocks, Kimhae area", *J. Geol. Soc. Korea*, **12**(4), 227-241 (in Korean with English abstract).

Lee, I.M. and Kim, D.H. (1999), "Parameter estimation using extended Bayesian method in tunnelling", *Comput. Geotech.*, **24**(2), 109-124. https://doi.org/10.1016/S0266-352X(98)00031-7.

Lekhnitskii, S.G. (1963), *Theory of Elasticity of an Anisotropic Elastic Body*, Holen-Day, San Francisco, California, U.S.A.

Lewis, R.W., Schrefler, B.A. and Simoni, L. (1991), "Coupling versus uncoupling in soil consolidation", *Int. J. Numer. Anal. Meth. Geomech.*, **15**(8), 533-548. https://doi.org/10.1002/nag.1610150803.

Love, A.E.H. (1944), *A Treatise on the Mathematical Theory of Elasticity*, 4th Edition, Dover Publications, New York, New York, U.S.A.

Mohr, O. (1900), "Welche umstände bedingen die elastizitätsgrenze und den bruch eines materials?", *Zeitschrift des Vereines Deutscher Ingenieure*, **44**(45), 1524-1530, 1572-1577 (in German).

Neuzil, C.E. (2003), "Hydromechanical coupling in geologic processes", *Hydrogeol. J.*, **11**(1), 41-83. https://doi.org/10.1007/s10040-002-0230-8.

Noorishad, J., Mehran, M. and Narasimhan, T.N. (1982), "On the formulation of saturated-unsaturated fluid flow in deformable porous media", *Adv. Water Resour.*, **5**(1), 61-62. https://doi.org/10.1016/0309-1708(82)90030-6.

Nur, A. and Byerlee, J.D. (1971), "An exact effective stress law for elastic deformation of rock with fluids", *J. Geophys. Res.*, **76**(26), 6414-6419. https://doi.org/10.1029/JB076i026p06414.

Ouyang, Z. and Elsworth, D. (1993), "Evaluation of groundwater flow into mined panels", *Int. J. Rock Mech. Min. Sci. Geomech. Abstr.*, **30**(2), 71-79. https://doi.org/10.1016/0148-9062(93)90701-E.

Safai, N.M. and Pinder, G.F. (1979), "Vertical and horizontal land deformation in a desaturating porous medium", *Adv. Water Resour.*, **2**, 19-25. https://doi.org/10.1016/0309-1708(79)90003-4.

Sandhu, R.S. and Wilson, E.L. (1969), "Finite-element analysis of seepage in elastic media", *J. Eng. Mech. Div., Proc. Am. Soc. Civ. Eng.*, **95**(EM3), 641-652.

Terzaghi, K. (1925), *Erdbaumechanik auf Bodenphysikalischer Grundlage*, Franz Deuticke, Leipzig, Saxony, Germany.

Thompson, M. and Willis, J.R. (1991), "A reformation of the equations of anisotropic poroelasticity", *J. Appl. Mech., Trans. Am. Soc. Mech. Eng.*, **58**(3), 612-616. https://doi.org/10.1115/1.2897239.

Tran, A.T.P., Kim, A.R. and Cho, G.C. (2019), "Numerical modeling on the stability of slope with foundation during rainfall", *Geomech. Eng.*, **17**(1), 109-118. https://doi.org/10.12989/gae.2019.17.1.109.

Tu, Y., Zhong, Z., Luo, W., Liu, X. and Wang, S. (2016), "A modified shear strength reduction finite element method for soil slope under wetting-drying cycles", *Geomech. Eng.*, **11**(6), 739-756. https://doi.org/10.12989/gae.2016.11.6.739.

Ukritchon, B., Faustino, J.C. and Keawsawasvong, S. (2016), "Numerical investigations of pile load distribution in pile group foundation subjected to vertical load and large moment", *Geomech. Eng.*, **10**(5), 577-598. https://doi.org/10.12989/gae.2016.10.5.577.

van Genuchten, M.Th. (1980), "A closed-form equation for predicting the hydraulic conductivity of unsaturated soils", *Soil Sci. Soc. Am. J.*, **44**(5), 892-898. https://doi.org/10.2136/sssaj1980.03615995004400050002x.

Verruijt, A. (1969), *Elastic Storage of Aquifers*, in De Wiest, R.J.M. (Editor), *Flow through Porous Media*, Academic Press, New York, New York, U.S.A., 331-376.

Wang, C., Zhou, S., Wang, B., Guo, P. and Su, H. (2016), "Settlement behavior and controlling effectiveness of two types of rigid pile structure embankments in high-speed railways", *Geomech. Eng.*, **11**(6), 847-865. https://doi.org/10.12989/gae.2016.11.6.847.

Yeh, G.T. (1987), "FEMWATER: A finite element model of water flow through saturated-unsaturated porous media, first revision", Technical Report No. ORNL-5567/R1, Oak Ridge National Laboratory, Oak Ridge, Tennessee, U.S.A.

Yeh, G.T. (1999), *Computational Subsurface Hydrology: Fluid Flows*, Kluwer Academic Publishers, Norwell, Massachusetts, U.S.A.

Yeh, H.D., Lu, R.H. and Yeh, G.T. (1996), "Finite element modelling for land displacements due to pumping", *Int. J. Numer. Anal. Meth. Geomech.*, **20**(2), 79-99. https://doi.org/10.1002/(SICI)1096-9853(199602)20:2<79::AID-NAG808>3.0.CO;2-M.

Yu, S. (2018), "Limit analysis of a shallow subway tunnel with staged construction", *Geomech. Eng.*, **15**(5), 1039-1046. https://doi.org/10.12989/gae.2018.15.5.1039.

Zhang, H., Chen, Q., Chen, J. and Wang, J. (2017), "Application of a modified structural clay model considering anisotropy to embankment behavior", *Geomech. Eng.*, **13**(1), 79-97. https://doi.org/10.12989/gae.2017.13.1.079.

Zheng, G., Du, Y., Cheng, X., Diao, Y., Deng, X. and Wang, F. (2017), "Characteristics and prediction methods for tunnel deformations induced by excavations", *Geomech. Eng.*, **12**(3), 361-397. https://doi.org/10.12989/gae.2017.12.3.361.

CC